Image Processing based Quantitative Damage Evaluation in Composites with Long Pulse Thermography

[1]Zijun Wang, [2, 1]GuiYun Tian, [3]Michele Meo, [*3]Francesco Ciampa

[1]School of Aeronautics and Astronautics, University of Electronic Science and Technology of China, Chengdu 611731, China.

[2]School of Electrical and Electronic Engineering, Newcastle University, Newcastle upon Tyne NE1 7UR, UK.

[3]Materials and Structures (MAST) Centre, Department of Mechanical Engineering, University of Bath, Bath BA2 7AY, UK.

*Corresponding Author: f.ciampa@bath.ac.uk

ABSTRACT

Pulsed thermography is a contactless and rapid non-destructive evaluation (NDE) technique that is widely used for the inspection of fibre reinforced plastic composites. However, pulsed thermography uses expensive and specialist equipment such high-energy flash lamps to generate heat into the sample, so that alternative thermal stimulation sources are needed. Long pulse thermography was recently developed as a cost-effective solution to enhance the defect detectability in composites by generating step-pulse heat into the test sample with inexpensive quartz halogen lamps and measuring the thermal response during the material cooling down. This paper provides a quantitative comparison of long pulse thermography with traditional pulsed thermography and step heating thermography in carbon fibre and glass fibre composites with flat-bottomed holes located at various depths. The three thermographic methods are processed with advanced thermal image algorithms such as absolute thermal contrast, thermographic signal reconstruction, phase Fourier analysis and principal component analysis in order to reduce thermal image artefacts. Experimental tests have shown that principal component analysis applied to long pulse thermography provides accurate imaging results over traditional pulsed thermography and step heating thermography. Hence, this inspection technique can be considered as an efficient and cost-effective thermographic method for low thermal conductivity and low thermal response rate materials.

Keywords: Long Pulse Thermography; Infrared Thermography; Principal Component Analysis;

Thermographic Signal Reconstruction

1. INTRODUCTION

Active Infrared (IR) thermography is a contactless non-destructive evaluation (NDE) technique that has been developed in the early 1980s for the inspection of damaged components [1], [2], [3]. Nowadays, it is widely used at both research and industrial level due to its capabilities to perform remote inspection on large surfaces in a rapid and reliable way. Optical heaters are typical thermal excitation sources for IR thermography, although ultrasonic waves [4], [5], [6], [7] eddy currents [8], [9], [10], microwaves [11] and thermoresistive heating have also been recently used to generate heat in the test component [12], [13]. Among IR thermographic methods, pulsed (or flash) thermography (PT) is widely used in composite materials [14], [15], [16]. In PT, short duration flashes (ranging typically between 0.1 and 50 ms) are applied to the sample under inspection and the resulting thermal gradients at the sample's surface are measured with an IR camera in order to visualise the material damage. PT is particularly suitable in the presence of air gap caused by either near surface or internal defects (e.g. delamination), which prevents the heat flaw to propagate from the surface into the laminate bulk. However, PT is still limited by expensive thermographic equipment such high-energy flash light sources. For example, commonly used flash systems such as the TWI Thermoscope and the EH Pro 6000 HENSEL Studiotechnik lamps require more than 5 kW of power to generate 12 kJ [17] and 6 kJ [18] of energy, respectively. Moreover, the short duration of the thermal pulse applied to the composite material may not be sufficient to illuminate the damage, especially for deep-lying defects. Hence, alternative optical heat stimulation sources for thermography have been used in recent years. Periodic heating with a sinusoidally modulated tungsten-halogen flood lamp is employed for lock-in thermography [19], whereas non-stationary forms of thermal excitation are used for frequency modulated thermography [20]. Nevertheless, these thermographic techniques require powerful amplifiers and specialist equipment for accurate thermal excitation. A different and cost-effective solution would be to apply a step-pulse heat source with inexpensive 500 W quartz halogen lamps for a long period, typically seconds, thus enabling sufficient heat to illuminate the damage. This technique, known as step-heating thermography (SHT) [21], consists of measuring thermal signals directly during the application of the step-pulse [22], [23]. The main advantage of SHT is the high sensitivity to defects in low thermal conductivity and low thermal response rate materials such as carbon fibre (CFRP) and glass fibre (GFRP) reinforced plastic composites. In addition, SHT does not

require accurate synchronization of the thermal excitation with the IR acquisition system [24]. Almond et al. [25] recently proposed long pulse thermography (LPT) that uses step-pulse heat as in SHT but, in LPT, thermal images are measured during the cooling phase of the test piece after the thermal excitation. The authors tested LPT on both metallic and composite specimens by analysing the raw thermal data and compared its detection performance with PT. They found that the intensity of thermal excitation (i.e. the energy density) produced by LPT was higher than that achieved with PT.

However, to date, a quantitative comparison of the damage detection performance of LPT against PT and SHT for fibre-reinforced composites by using the state-of-the-art of signal processing algorithms for thermal data is still missing. Advanced post-processing techniques are reported for optical IR thermography such as Absolute Thermal Contrast (ATC), Thermographic Signal Reconstruction (TSR), Phase Fourier Analysis (PFA) and Principal Component Analysis (PCA) [26], [27], [28], [29], [30]. These data processing methods have shown to provide enhanced detection and quantification of material damage in the presence of thermal image artefacts caused by non-uniform heating of the test surface, anisotropic diffusivities and additive noise such as environmental reflections and emissivity variations [31].

This paper presents a quantitative experimental analysis of LPT for the assessment of material damage in both CFRP and GFRP composite laminates. LPT is here compared with PT and SHT in combination with the four above mentioned data processing techniques. It was found that for fibre reinforced polymer specimens, LPT provides great advantages over traditional heating methods, especially with PCA processing. The overall structure of this paper is as follows: the post-processing methods of thermal data are presented in Section 2. The experimental set-up and thermal excitation processes are summarized in Section 3. Section 4 provides the experimental thermal results of CFRP and GFRP test samples. Finally, the conclusions are outlined in Section 5.

2. POST-PROCESSING METHODS OF THERMAL DATA

Various image post-processing algorithms have been developed to analyse thermal data recorded by the IR camera and enhance the quality of thermal images for damage detection. The principal objectives of image processing are the identification of hot spots and the extraction of damage features. A brief description of the four signal processing methods used in this paper, namely ATC, TSR, PFA and PCA, is provided in the following sub-Sections.

2.1 Absolute Thermal Contrast

Absolute thermal contrast (ATC) is the most commonly used signal processing technique to enhance the contrast of surface temperature between a sound (undamaged) area and a defect area. The absolute thermal contrast $C_{[i,j]}(t)$ is defined as [32]:

$$C_{[i,j]}(t) = T_{[i,j]}(t) - Ts_{[i,j]}(t), \quad (1)$$

where $T_{[i,j]}(t)$ is the temperature at time *t*, $Ts_{[i,j]}(t)$ is temperature of a sound area as result of calculating the average temperature of the specimen surface in various pixels, and $[i,j]$ is the spatial location of a generic pixel (either defective or not) within the field of view of the IR camera. ATC was here applied to LPT, PT and SHT.

2.2 Thermography Signal Reconstruction

The Thermography signal reconstruction (TSR) technique was originally developed for PT in order to process each pixel's time history from the thermographic image sequence. TSR is based on the assumption that temperature profiles for non-defective pixels should follow the approximated one-dimensional (1D) solution of the Fourier equation in its logarithmic form [33]. However, to fit the approximated solution, the logarithmic time response is linearized with the following *n*-th degree polynomial function:

$$\ln(T_{[i,j]}) = a_0 + a_1 \ln(t) + a_2[\ln(t)]^2 + \cdots + a_n[\ln(t)]^n, \quad (2)$$

where, similarly to Eq. (1), $T_{[i,j]}$ is the temperature increase as a function of time for each pixel $[i,j]$ and $a_0[i,j], a_1[i,j], \ldots a_n[i,j]$ are the polynomial coefficients. The choice of the optimal degree of the polynomial function was found to be up to the seventh degree [34]. Both first time- and second time-derivatives achieved directly on the polynomial provide a higher signal-to-noise (SNR) ratio and enhance damage detectability [35], [36]. Similarly to the absolute thermal contrast method, TSR was applied to LPT and thermal results were compared with PT and SHT.

2.3 Phase Fourier Analysis (PFA)

Phase Fourier Analysis (PFA) (e.g. Pulsed Phase Thermography) is widely used to produce phase images from thermal data [31]. In PFA, each thermal signal is transformed from the time domain to the frequency one using the well-known discrete Fourier transform (DFT) [37]:

$$F_n = \Delta t \sum_{k=0}^{N-1} T(k\Delta t) exp - \frac{j2\pi k}{N} = \mathrm{Re}_n + \mathrm{Im}_n, \quad (3)$$

where $j = \sqrt{-1}$ is the imaginary number, n is the frequency increment ($n = 0,1,\dots,N$), Δt is the sampling time interval and Re and Im are the real and imaginary part of the Fourier transform, respectively, with the phase $\Phi_n = tan^{-1}(\mathrm{Im}_n/\mathrm{Re}_n)$. The phase image (phasegram) is particularly of interest for LPT, PT and SHT as it is less affected by non-uniform heating, environmental reflections and emissivity variations.

2.4 Principal Component Analysis (PCA)

Signal decomposition by time-frequency and time scale representation is an essential element of the thermal signal analysis. Standard Fourier transform, as in PFA, expresses any arbitrary periodic function of time as the sum of a set of sinusoids. Hence, the characteristics of non-stationary monotonic signals as in PT or LPT may potentially be hindered [38]. The principal component analysis (PCA) is a multivariate signal processing technique that can be considered as an alternative to PFA and it is used to reduce the dimension of acquired thermal signals by projecting the original data onto a system of orthogonal components [39], [40]. In this manner, desirable signal features can be extracted from the thermal image sequence and undesirable noise effects can be filtered out. The thermal image sequence is a three-dimensional (3D) image matrix, **A**, consisting of P image frames with $M \times N$ pixels per frame, which is defined as follows:

$$\boldsymbol{A}_p = \begin{bmatrix} a_{11} & \cdots & a_{1N} \\ \vdots & \ddots & \vdots \\ a_{M1} & \cdots & a_{MN} \end{bmatrix}, \; p = 1,2,\dots,P. \quad (4)$$

In order to apply the PCA, a vectorisation operation is initially performed to convert the 3D matrix $\mathbf{A}_p$ into a two-dimensional (2D) sample vector **X**. Such a vectorisation is achieved by stacking each image frame by column

$$\mathbf{x}_p = (a_{11} \cdots a_{M1} \cdots a_{1N} \cdots a_{MN})^T, \; p = 1,2,\dots,P \quad (5)$$

and by combining the new P sample vectors $\mathbf{x}_p$ into the sample matrix **X** of dimensions $[MN \times P]$:

$$\mathbf{X} = (\mathbf{x}_1, \mathbf{x}_2, \cdots, \mathbf{x}_P). \quad (6)$$

According to Rajic [39], a normalisation operation is performed on the matrix **X** in order to reduce side effects caused by uneven heating and noise from the surrounding environment. Such a normalisation process is accomplished by subtracting from each column of the matrix **X** the mean value $\bar{\mathbf{x}}$, and calculating the covariance matrix $\widehat{\mathbf{X}}$ of dimensions $[MN \times MN]$:

$$\widehat{\mathbf{X}} = \frac{1}{P-1}\sum_{p=1}^{P}(\mathbf{x}_P - \overline{\mathbf{x}})\,(\mathbf{x}_P - \overline{\mathbf{x}})^T, \tag{7}$$

with $\overline{\mathbf{x}}_p = 1/P\sum_{p=1}^{P}(\mathbf{x}_P)$. Once thermal data are normalised, a singular value decomposition (SVD) operation is performed on the covariance matrix to calculate the principal components as follows:

$$\widehat{\mathbf{X}} = \mathbf{USV}^T. \tag{8}$$

In the SVD process of Eq. (8), the matrix **U** consists of orthogonal functions representing the spatial variations of the thermal data set. Each column of **U** provides the coordinates of thermal signals in the space of principal components. The matrix **S** is a diagonal matrix with singular values on its diagonal that are arranged in a descending order. These singular values in **S** are the nonzero square root of the eigenvalue $\widehat{\mathbf{X}}^T\widehat{\mathbf{X}}$ for the corresponding eigenvectors in the matrix **V**. The first three columns of matrix **U** are known as empirical orthogonal functions (EOF),

$$\mathbf{U}_i = (u_{1,i}\ \ u_{2,i}\ldots\ u_{MN,i})^T \quad i = 1,2,3 \tag{9}$$

and represent nearly 80% to 90% of the variation of the measured thermal data associated with the spatial variation of the material defect. Hence, these vectors are used in the PCA process to rebuild the final spatial image matrices $\mathbf{B}_i$ associated with the first principal components as follows:

$$\boldsymbol{B}_i = \begin{bmatrix} u_{1,i} & u_{M+1,i} & \cdots & u_{(N-1)M+1,i} \\ u_{2,i} & u_{M+2,i} & \cdots & u_{(N-1)M+2,i} \\ \vdots & \vdots & \ddots & \vdots \\ u_{M,i} & u_{2M,i} & \cdots & u_{MN,i} \end{bmatrix} \quad i = 1,2,3. \tag{10}$$

3. EXPERIMENTAL TESTS

3.1 Experimental Set-up

Two composite plates with flat-bottomed back-drilled hole defects were tested in order to provide a quantitative assessment of LPT in combination with the four above mentioned signal processing techniques. Flat bottom holes were here investigated as they allow simulating either in-plane delamination defects or material loss damage [41]. The first sample was a carbon fibre reinforced plastic (CFRP) composite of dimensions 150 mm × 100 mm × 7.3 mm. Eight flat-bottomed holes were drilled with a constant diameter, D, of 6 mm at various depths, d, ranging between 0.8 mm and 2.5 mm. The second specimen was a glass fibre reinforced plastic (GFRP) laminate with dimensions of 150 mm × 100 mm × 3 mm. Twelve flat-bottomed holes were drilled with three sets of diameters (2.5 mm, 5 mm and 10 mm) at four depths (i.e. 0.5 mm, 1 mm, 1.5 mm and 2 mm, respectively). Figure 1 illustrates the location of defects and their diameters within each laminate and Figure 2 shows the photographs of the test specimens. No further information was provided by the

manufacturer about the lay-up of composite samples.

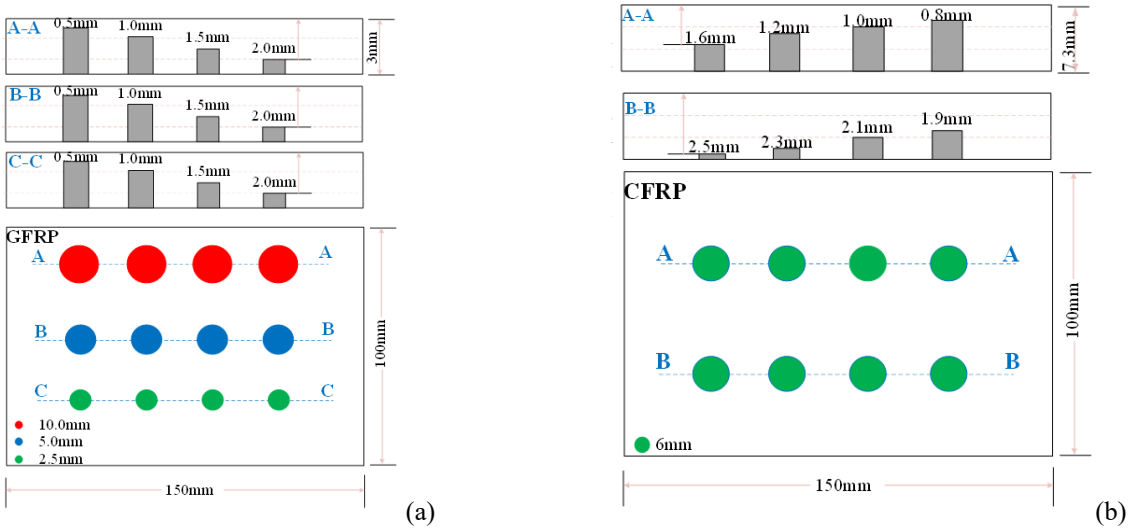

Figure 1. Illustration of diameters of flat-bottomed hole defects and their in-depth location in the GFRP (a) and CFRP (b) test specimens.

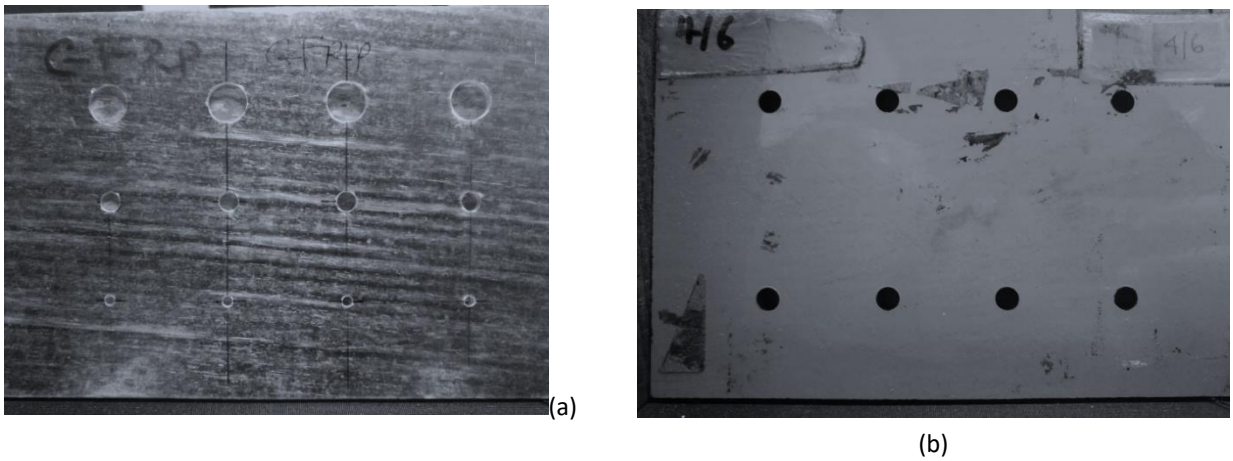

Figure 2. Real flat-bottomed hole defects in the GFRP (a) and CFRP (b) test specimens.

For the PT experiments, a 6 kJ Xenon EH Pro 6000 HENSEL Studiotechnik flash lamp was driven by a Hensel TRIA 600 S generator in order to produce a 5 ms width heating pulse. In agreement with Almond et al. [24], such a flash lamp excitation system is capable of delivering an energy density of ~3 kJm^{-2} when located at a distance of ~30 cm from the surface of the test sample. For the LPT and SHT experiments, a pair of 1 kW quartz halogen lamps were used, which are capable of delivering a power density of ~2kWm^{-2}. The heating period was controlled by two drop plate shutters capable of shielding the test piece from the lamps' residual infrared emissions (afterglow effect) after they were switched off. These shutters were elastically accelerated and closed within the IR camera time frame. The IR camera was a CEDIP (now FLIR) Jade MWIR 3-5 µm camera with a focal plane array

size of 320 × 240 pixels and a sensitivity of 20 mK (NEDT). As in the general practise of flash thermography, no shutters were used in PT tests. The experimental set-ups of the three thermographic methods are shown in Figure 3.

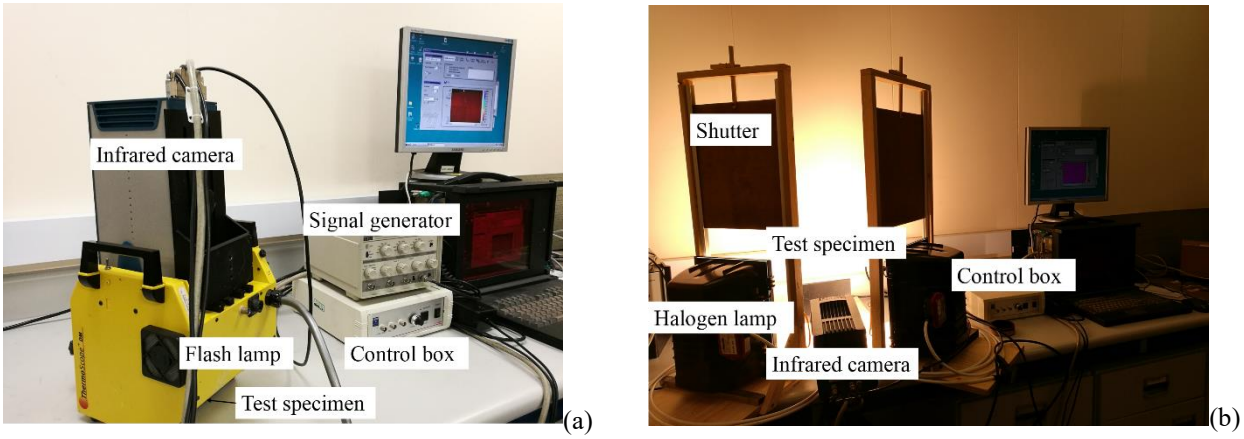

Figure 3. Experimental set-up for PT (a) and for both SHT and LPT (b).

In the LPT and PT experiments, the camera recorded the infrared thermal images during the cooling period at a rate of 50 images per second and an integration time of 400 μs. For the SHT tests, the camera acquired images during the heating period at the same rate and integration time. The 3D images of thermal signals were post-processed with user interface algorithms developed in MATLAB software. In all thermographic tests, the IR camera was placed opposite to the specimen under investigation at a distance of ~30 cm. The two lamps in the SHT and LPT tests were located on both sides of the camera at an angle of 45° from the specimen. This position of lamps allowed reducing thermal reflections into the camera, thus enhancing the quality of measured data.

3.2 Thermal Excitation Process

As reported in Section 3.1, a 5 ms flash heat pulse was transmitted in PT tests and the IR images were recorded after the pulse for 30 s. Similarly to Almond et al. [24], a 7 s long pulse heat was used in both LPT and SHT. Whilst in LPT the IR camera acquired the thermographic image sequence for 30 s (cooling time) after shutters were switched off, in SHT, the IR camera recorded the images during the heating period (i.e. up to 7 s). Figure 4 shows the temperature profile of a pixel in the image sequence during both the heating and cooling phases of SHT and LPT. The background temperature (or the initial temperature) of the test specimen is shown as the point A in Figure 4, whereas the point B corresponds to the end of the step-heating phase (i.e. the point when the maximum temperature is

reached). After heating, the temperature profile begins to decrease and then settles at a temperature C.

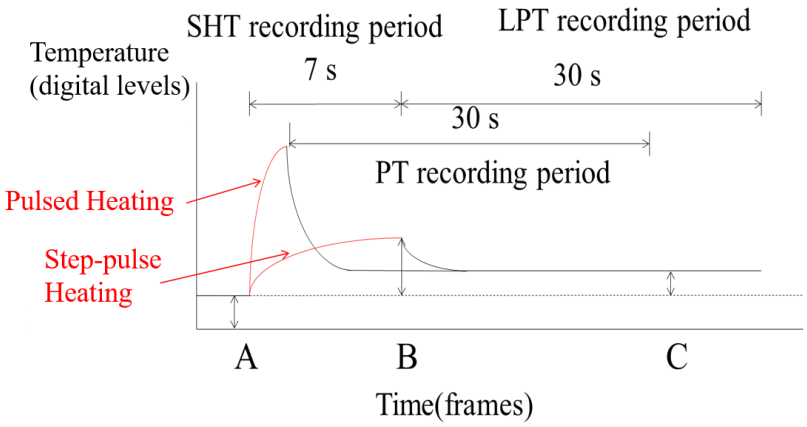

Figure 4. Temperature profile of the thermal imaging process for both LPT and SHT.

4. EXPERIMENTAL RESULTS

Thermographic experiments of LPT, SHT and PT were carried out on the GFRP and CFRP specimens with the same procedures and data analysis techniques. The recorded raw images were then post-processed in order to evaluate the damage detection performance of LPT against traditional optical thermographic methods. In the following thermal image results, the detected defects are plotted by solid lines and the undetected ones are shown by dashed lines. With reference to Section 2, four signal post-processing techniques were here investigated. The ATC method was computed by calculating the difference between the surface temperature of the defect and sound areas. The TSR processing was applied to all raw sequences by using up to the 7th degree of logarithmic polynomial coefficients $a_n(n = 0,1,\cdots,7)$ in Eq. (2). In PFA, IR thermal signal data were computed using the 1D Fourier transform in order to enable the thermal phase information and enhance the visibility of deeper defects by suppressing uneven heating effects [42]. Finally, in the PCA method, the raw data were compressed to create new 2D images matrices using the second and third principal components by reconstructing the final spatial image matrices $\mathbf{B}_2$ and $\mathbf{B}_3$ in Eq. (10), respectively.

4.1 Thermographic Results on the GFRP Composite

Figure 5 compares raw thermographic sequences obtained during the cooling phase for PT and LPT at three different times (5 s, 15 s and 25 s, respectively). As the cooling time increased, the defect signatures of both PT and LPT vanished, with LPT capable of revealing more defects than PT. For

example, at time t = 5s, seven defects (i.e. four with 10 mm diameter and three with 5 mm diameter) were detected with LPT, whereas only two with the diameter of 10 mm were visible with PT [Figure 5(a)-(b)]. With reference to Almond et al. [24] and Krankenhagen and Maierhofer [18], these results can be explained by the higher excitation energy achieved by LPT in comparison with that of PT. Indeed, whilst the PT excitation system provides an overall energy density of ~3 kJm^{-2}, the power density of the LPT achieved with two quartz halogen lamps is ~2kWm^{-2} that, for 7 s excitation, corresponds to a total long pulse excitation energy of ~14kWm^{-2}. As it can be seen from Figure 5, with simple raw data (i.e. with no post-processing technique applied), LPT was found to be more effective than PT in a low thermal conductivity and low thermal response rate material such as the GFRP laminate.

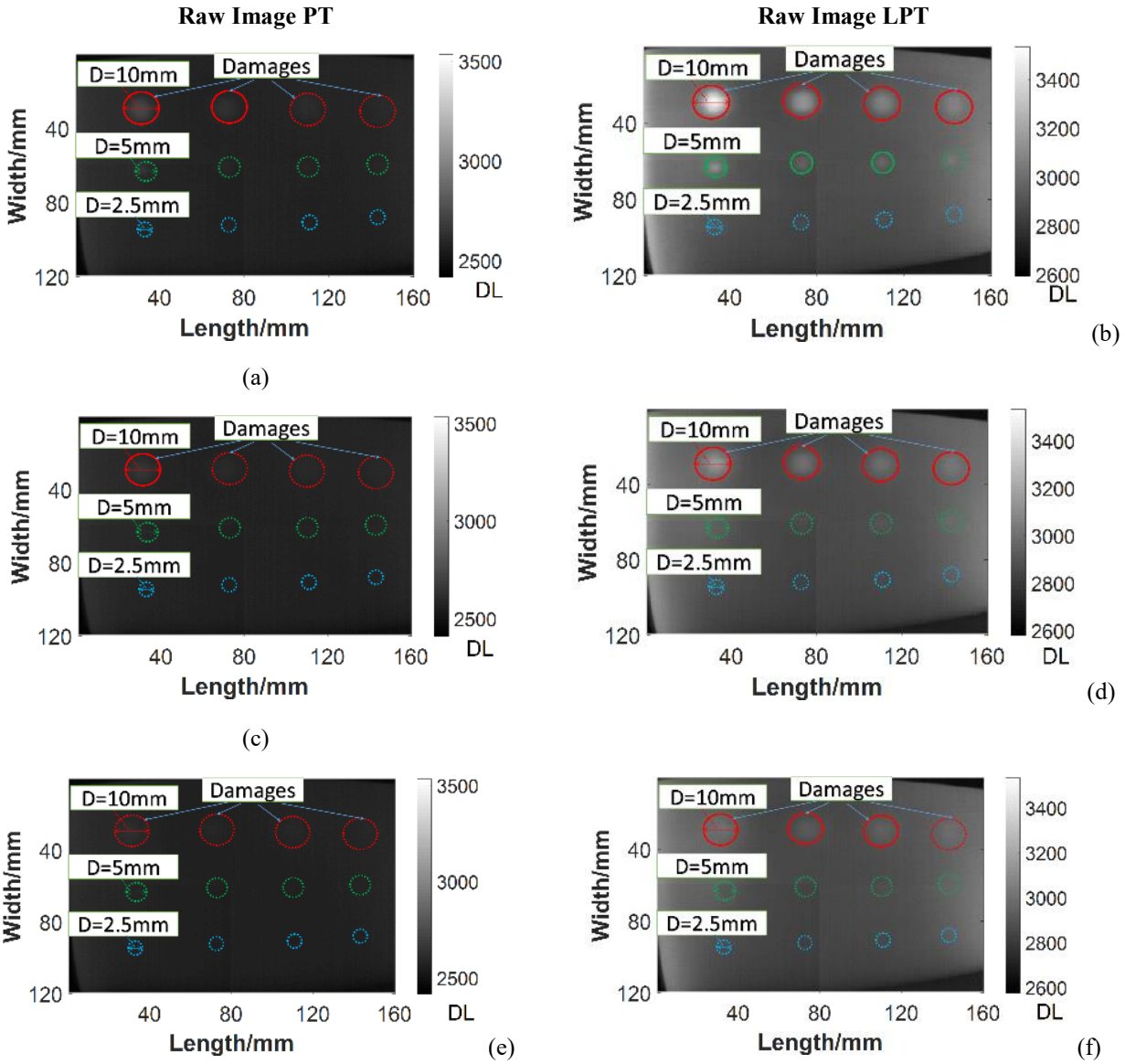

Figure 5. PT and LPT raw images of GFRP tests obtained at the time t = 5 s (a) - (b), t = 15 s (c) - (d) and t = 25 s (e) -

(f) after heating. Detected defects in the images are plotted by solid lines and the undetected ones are shown by dashed lines.

Figure 6 presents the raw sequence data of SHT during the heating step-pulse of 7 s. At the time t = 1 s, only one defect with diameter of 10 mm was detected, whereas seven flaws (i.e. three with D = 10 mm, two with D = 5 mm and two with D = 2.5 mm) became visible at t = 7 s. Hence, whilst in PT and LPT tests associated with the thermal cooling of the sample, the earliest times revealed more detectable defects, in SHT tests, instead, later heating times were used for damage assessment.

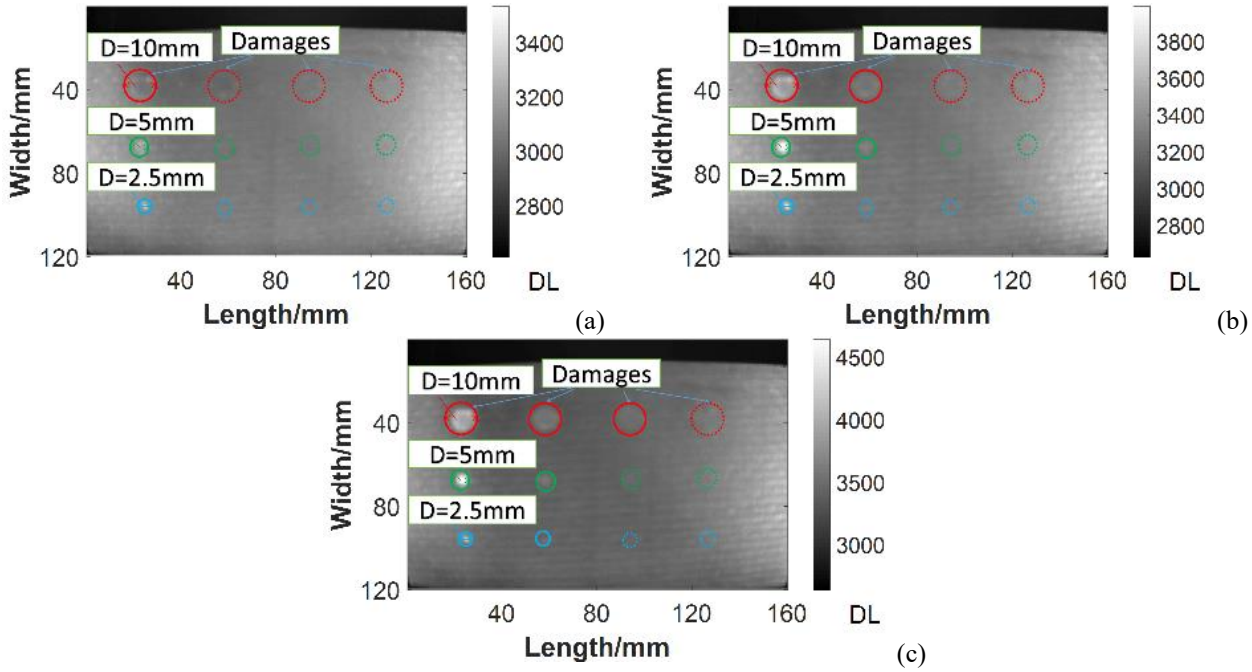

Figure 6. SHT raw images of GFRP tests obtained at the heating time of t = 1 s (a), t = 5 s (b) and t = 7 s (c). Detected defects in the images are plotted by solid lines and the undetected ones are shown by dashed lines.

Figure 7 shows the raw apparent temperature (in digital level) measured on defect pixels (with different diameters of the flat-bottomed holes) and on the sound area pixel with PT, SHT and LPT. The central point of the damage was used to generate thermal histories.

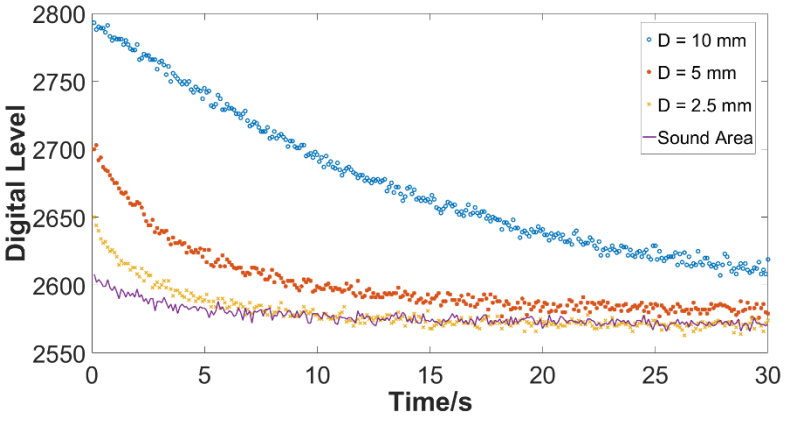

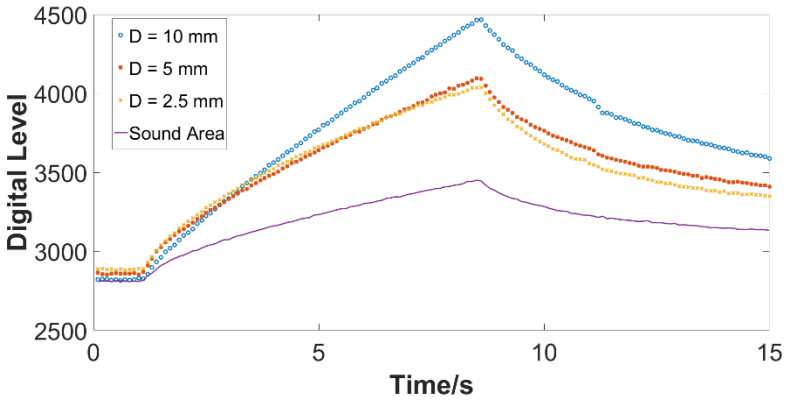

(b)

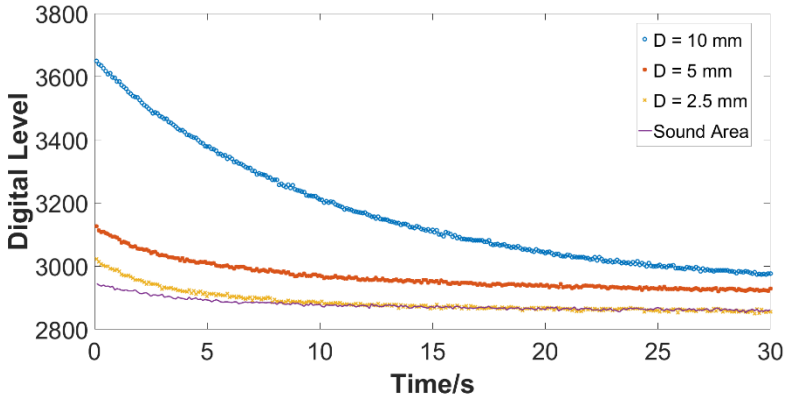

(c)

Figure 7. Time history of the apparent raw temperature data (in digital level) of PT (a), SHT (b) and LPT(c) for the GFRP sample. The heating time for PT is 5 ms, whereas for both SHT and LPT is 7 s. The depth of flat-bottomed hole defects was set constant at 1 mm.

Figure 8 shows the image results of post-processing techniques applied to PT, SHT and LPT, whereas Table 1 reports the total identified defects by each signal processing method on the GFRP sample. The four post-processing techniques enabled great advantage over the raw data images for the detection of material defects (see Figures 5 and 6), as they allowed revealing the presence of all flat-bottomed holes with 10 mm diameters. Only defects with small diameters and in-depth location were difficult to detect. As a result of comparison tests, the proposed LPT was more sensitive to small and in-depth damage than PT and SHT. Moreover, the image results of Figure 7 and Table 1 illustrated that PCA applied to LPT was the only technique capable of identifying eleven defects (out of twelve). For the PCA analysis, only the thermal results achieved with the second EOF represented by the matrix $\mathbf{B}_2$ were displayed. The phasegrams obtained with PFA technique showed, instead, that this signal processing method was more effective with PT at the thermal frequency of 0.06 Hz, whilst TSR performed better with SHT and LPT. For the implementation of TSR, the third degree of logarithmic polynomial coefficients was used for PT and LPT, whilst the fourth degree was employed

for SHT.

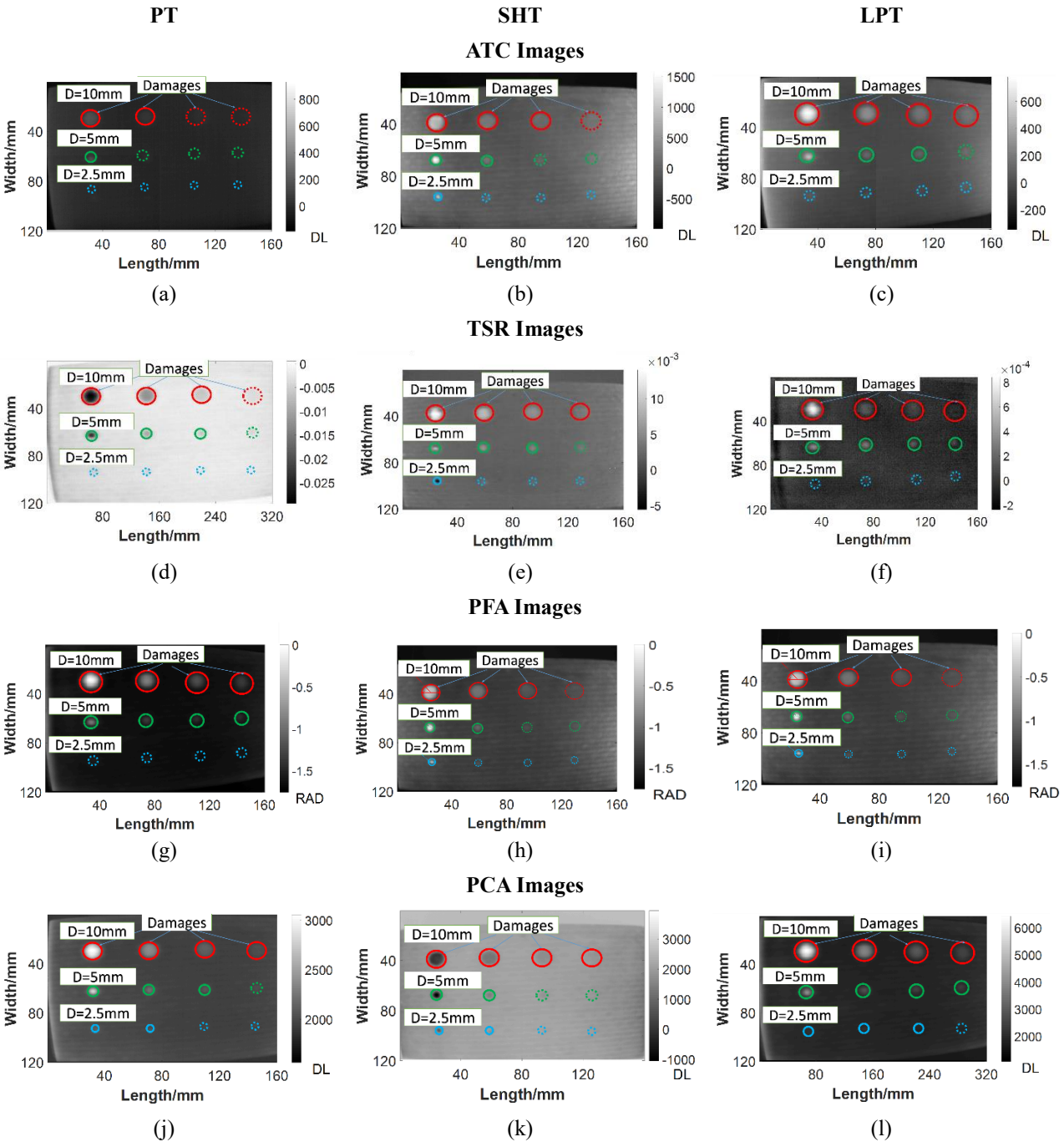

Figure 8. Signal processing methods applied to PT, SHT and LPT on the GFRP sample. The ATC images were obtained at the time $t = 2$ s for PT (a), $t = 7$ s for SHT (b) and $t = 2$ s for LPT (c). The TSR images were achieved with the coefficients a_3 for PT (d), a_4 for SHT (e) and a_3 for LPT (f). The PFA images were obtained at the thermal frequencies of 0.06 Hz for PT (g), 0.3 Hz for SHT (h) and 0.03 Hz for LPT (i). The PCA images were achieved from the matrix $\mathbf{B}_2$ associated with the 2nd principal component for PT (j), SHT (k) and LPT (l). Detected defects in the images are plotted by solid lines and the undetected ones are shown by dashed lines.

Tab.1. Summary of detected defects in the GFRP specimen.

Post-processing Methods	**PT**		**SHT**		**LPT**	
Raw Data Images	**2**	2 x D = 10.0 mm	**7**	4 x D = 10.0 mm	**7**	3 x D = 10.0 mm

		0 x D = 5.0 mm		3 x D = 5.0 mm		2 x D = 5.0 mm
		0 x D = 2.5 mm		0 x D = 2.5 mm		2 x D = 2.5 mm
ATC	**3**	2 x D = 10.0 mm	**6**	3 x D = 10.0 mm	**7**	4 x D = 10 mm
		1 x D = 5.0 mm		2 x D = 5.0 mm		3 x D = 5.0 mm
		0 x D = 2.5 mm		1 x D = 2.5 mm		0 x D = 2.5 mm
TSR	**6**	3 x D = 10.0 mm	**8**	4 x D = 10.0 mm	**8**	4 x D = 10.0 mm
		2 x D = 5.0 mm		3 x D = 5.0 mm		4 x D = 5.0 mm
		1 x D = 2.5 mm		1 x D = 2.5 mm		0 x D = 2.5 mm
PFA	**8**	4 x D = 10.0 mm	**6**	3 x D = 10.0 mm	**6**	3 x D = 10.0 mm
		4 x D = 5.0mm		2 x D = 5.0 mm		2 x D = 5.0 mm
		0 x D = 2.5 mm		1 x D = 2.5 mm		1 x D = 2.5 mm
PCA	**9**	4 x D = 10.0 mm	**8**	4 x D = 10.0 mm	**11**	4 x D = 10.0 mm
		3 x D = 5.0mm		2 x D = 5.0 mm		4 x D = 5.0 mm
		2 x D = 2.5 mm		2 x D = 2.5 mm		3 x D = 2.5 mm

It should be finally noted that the ratio “defect depth/diameter” is commonly used as an indicator for the accuracy of optical IR thermography concerning defect dimensions and in-depth location [43]. Generally, damage becomes difficult to be detected if this ratio is ≥ 1. As illustrated in Figure 1, the ratio of depth/diameter of the GFRP sample ranged between 0.05 and 0.8 and the only undetectable defect with LPT and PCA was the flat-bottomed hole with depth/diameter ratio equal to 0.8.

4.2 Thermographic Results on the CFRP Composite

Figure 9 compares the raw thermographic sequences obtained with PT and LPT tests on the CFRP sample. This specimen has larger thickness than the GFRP sample examined in Section 4.1 and has higher thermal effusivity. By analysing only raw images, no defects were detected with PT as the energy density on the CFRP sample’s surface obtained with the optical flash was not sufficient to generate thermal gradients at the damage location above the sensitive limit of the IR camera. At early times (5 s) after the long pulse excitation, LPT was the only technique able to reveal three out of eight defects with depths d = 0.8 mm, d = 1 mm and d = 1.2 mm [Figure 9(b)]. As the cooling time increased, the propagation of thermal waves within the specimen became uniform and no further defects could be identified.

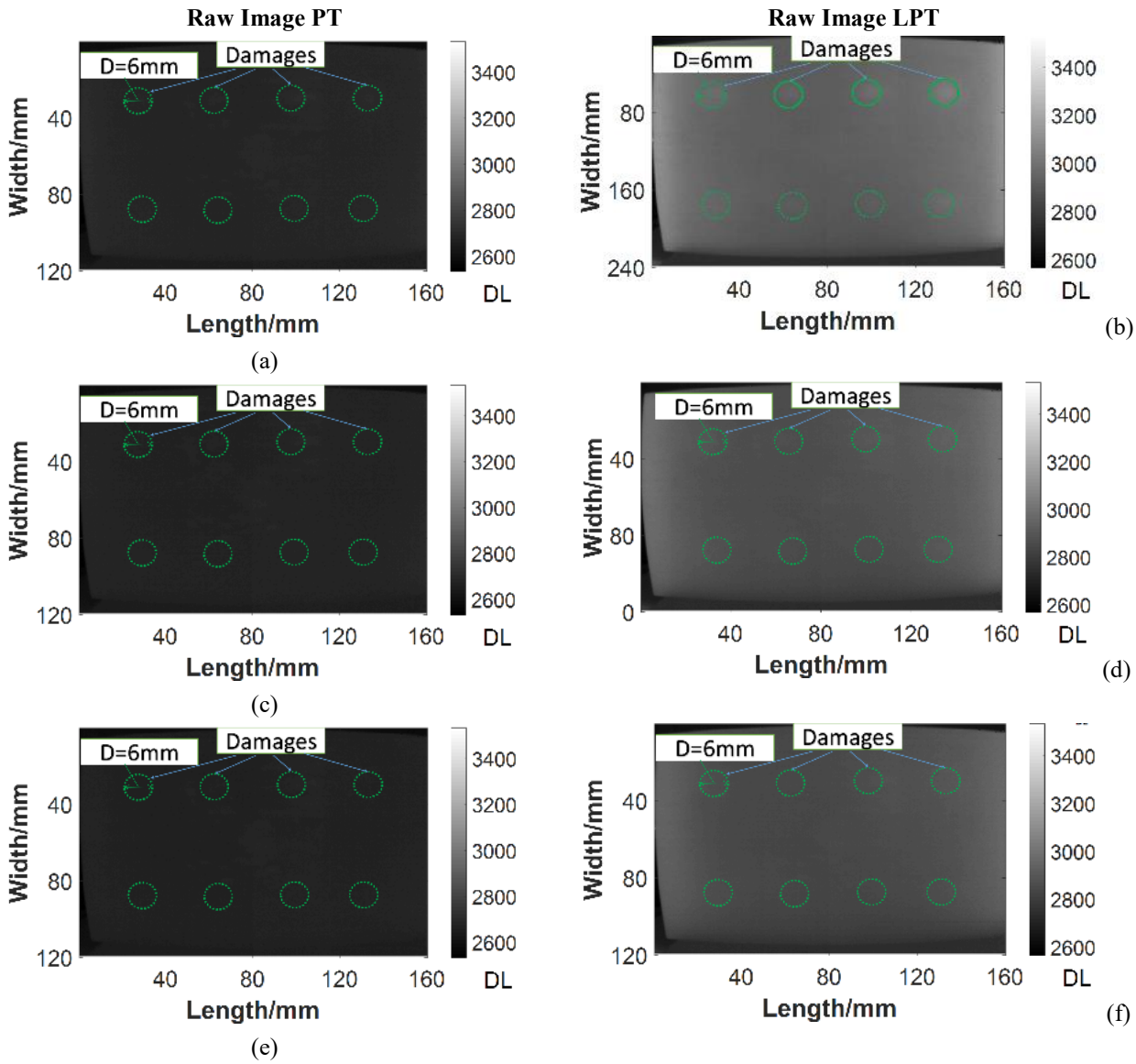

Figure 9. PT and LPT raw images of CFRP tests obtained at the time t = 5 s (a) - (b), t = 15 s (c) - (d) and t = 25 s (e) - (f) after heating. Detected defects in the images are plotted by solid lines and the undetected ones are shown by dashed lines.

In the case of SHT shown in Figure 10, later heating times were used in the raw images to retrieve thermal differences between pixels on defect and non-defect areas. Particularly, at the time t = 7 s, only the defect with depth d = 0.8 mm was detected [Figure 10(c)].

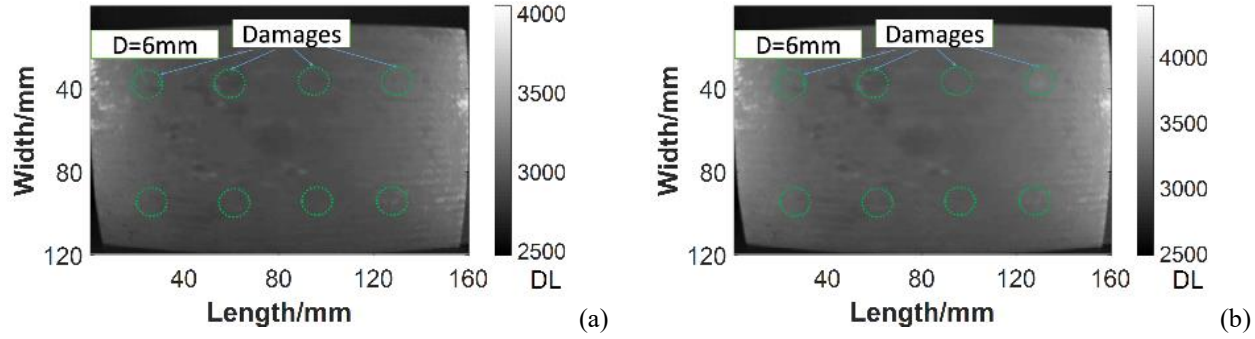

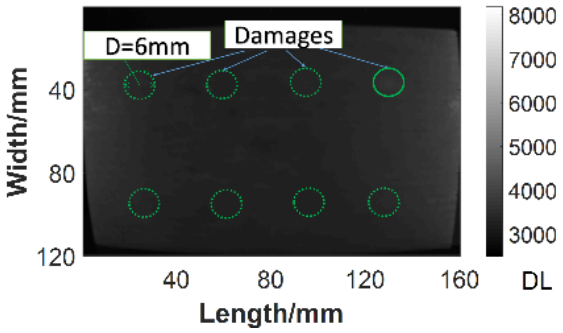

(c)

Figure10. SHT raw images of CFRP tests obtained at the heating time of t = 1 s (a), t = 5 s (b) and t = 7 s (c). Detected defects in the images are plotted by solid lines and the undetected ones are shown by dashed lines.

Similarly to Figure 7, Figure 11 depicts the raw apparent temperature (in digital level) measured on the defect pixel (with different diameters of the flat-bottomed holes) and on the sound area with PT, SHT and LPT for the CFRP test sample.

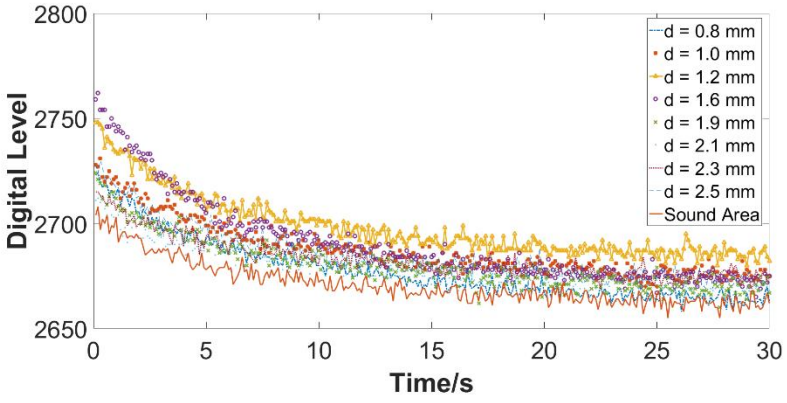

(a)

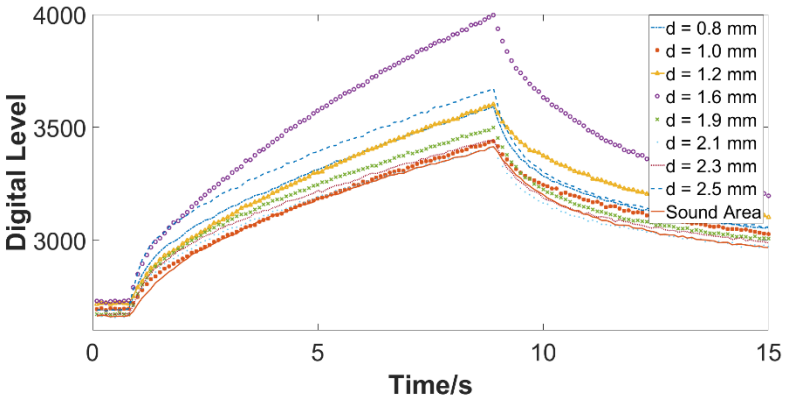

(b)

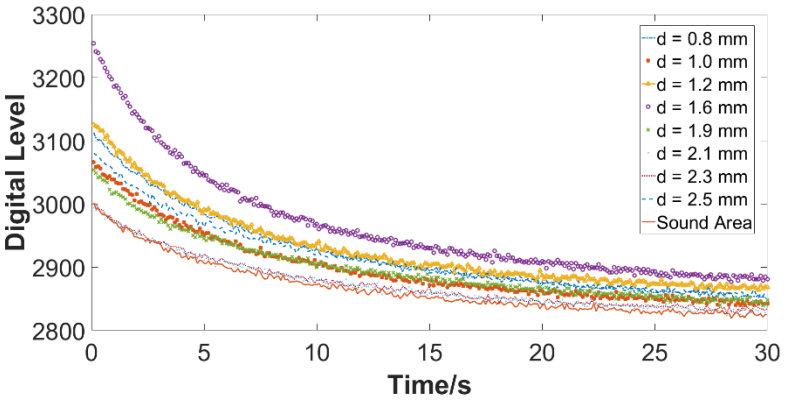

(c)

Figure 11. Time history of the apparent raw temperature data (in digital level) of PT (a), SHT (b) and LPT(c) for the CFRP sample. Similarly to Figure 7, the heating time for PT is 5 ms, whereas for both SHT and LPT is 7 s.

Post-processing techniques of thermal data were necessary on the CFRP specimen to reveal the presence of more defects. The processed images are shown in Figure 12 and the total number of detected defects is reported in Table 2. Similarly to the GFRP sample, the ATC technique provided little advantage compared with raw data images as only three flat bottomed holes were identified with LPT, only one damage was detected with SHT and no defects were visualised with PT. Unlike the GFRP sample, the phasegrams of PFA revealed more defects with SHT and LPT (four flaws at the thermal frequencies of 0.6 Hz and 0.03 Hz, respectively) than PT (three damages at the thermal frequency of 0.03 Hz). TSR results showed that six flaws were detected with LPT and only four with SHT using the third degree of the logarithmic polynomial coefficient. The performance of TSR was, instead, fairly poor with PT, for which the second degree polynomial coefficient provided the imaging of a single flat-bottomed hole. PCA, conversely, allowed detecting four defects with PT and all eight flat-bottomed holes with LPT by using the third principal component represented by the matrix $\mathbf{B}_3$.

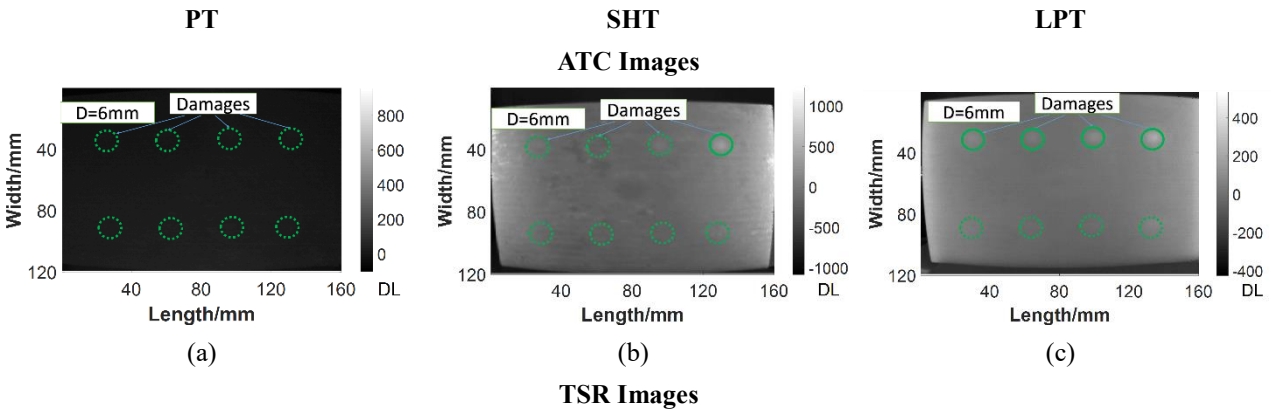

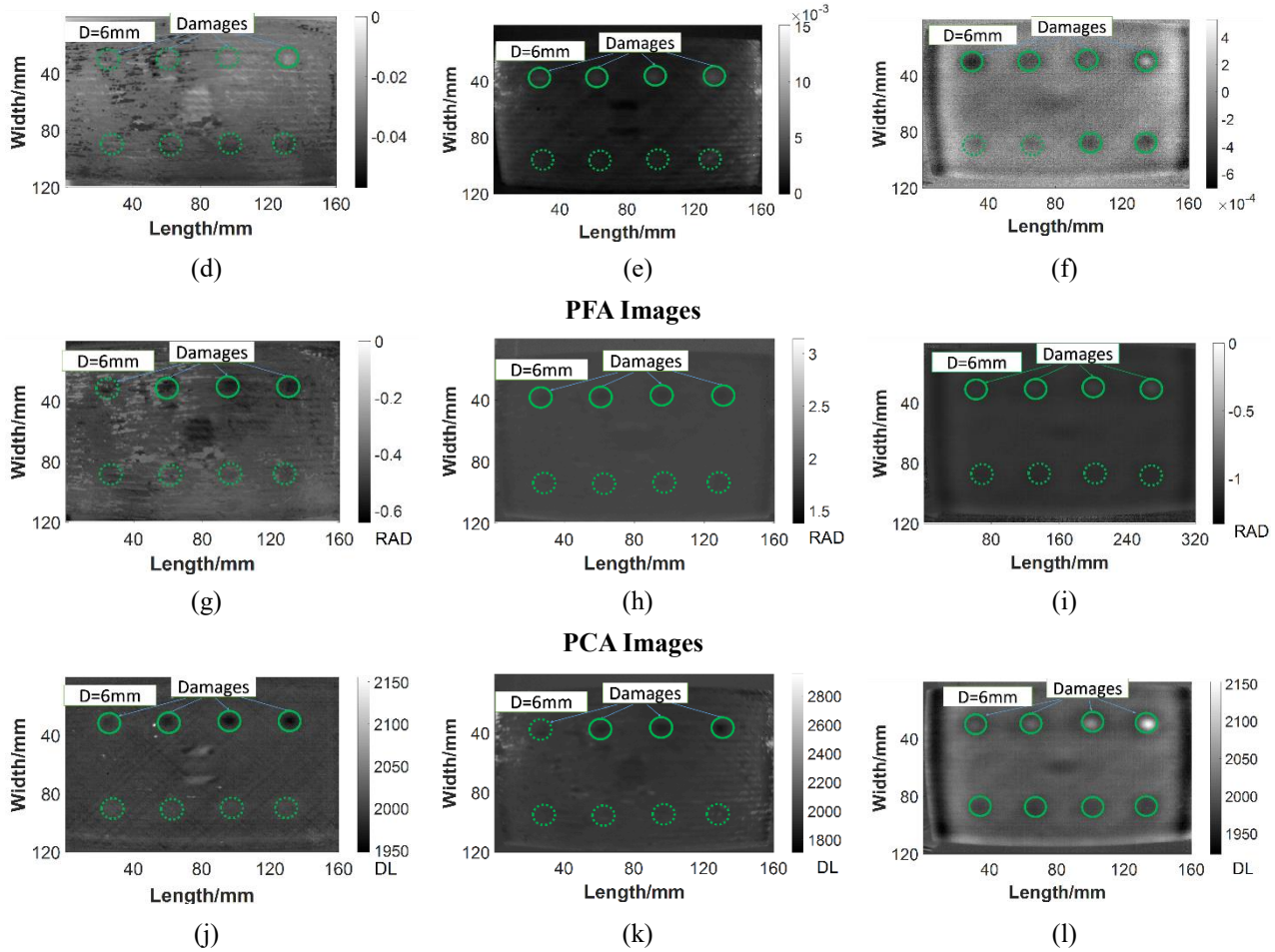

Figure 12. Signal processing methods applied to PT, SHT and LPT on the CFRP sample. The ATC images were obtained at the time $t = 2$ s for PT (a), $t = 7$ s for SHT (b) and $t = 2$ s for LPT (c). The TSR images were achieved with the coefficients a_2 for PT (d), a_3 for SHT (e) and a_3 for LPT (f). The PFA images were obtained at the thermal frequencies of 0.03 Hz for PT (g), 0.6 Hz for SHT (h) and 0.03 Hz for LPT (i). The PCA images were achieved from the matrix $\mathbf{B}_3$ associated with the 3rd principal component for PT (j), SHT (k) and LPT (l). Detected defects in the images are plotted by solid lines and the undetected ones are shown by dashed lines.

Tab. 2. Summary of detected defects in the CFRP specimen.

Post-processing Method	**PT**		**SHT**		**LPT**	
Raw Data Images	**0**	No defects	**1**	d = 0.8 mm	**3**	d = 0.8 mm
						d = 1.0 mm
						d = 1.2 mm
ATC	**0**	No defects	**1**	d = 0.8 mm	**4**	d = 0.8 mm
						d = 1.0 mm
						d = 1.2 mm
						d = 1.6 mm
TSR	**1**	d = 0.8 mm	**4**	d = 0.8 mm	**6**	d = 0.8 mm

				d = 1.0 mm		d = 1.0 mm
				d = 1.2 mm		d = 1.2 mm
				d = 1.6 mm		d = 1.6 mm
						d = 1.9 mm
						d = 2.1 mm
PFA	**3**	d = 0.8 mm	**4**	d = 0.8 mm	**4**	d = 0.8 mm
		d = 1.0 mm		d = 1.0 mm		d = 1.0 mm
		d = 1.2 mm		d = 1.2 mm		d = 1.2 mm
				d = 1.6 mm		d = 1.6 mm
PCA	**4**	d = 0.8 mm	**3**	d = 0.8 mm	**8**	All defects
		d = 1.0 mm		d = 1.0 mm		
		d = 1.2 mm		d = 1.2 mm		
		d = 1.6 mm				

As shown in Figure 1, the ratio of depth/diameter of the CFRP sample ranged from 0.13 to 0.42 and all defects in the CFRP specimen were detected. Hence, LPT with PCA can be considered as a valid alternative to standard optical IR thermography in low thermal conductivity and low thermal response rate materials such fibre reinforced polymer composites. Indeed, this technique requires less expensive quartz halogen lamps than specialist 6 kJ flash lamps used in PT (~100 times cheaper [25]) and it does not require accurate synchronization of excitation and IR imaging.

5. CONCLUSIONS

This work presented the damage detection performance of long pulse thermography over traditional step heating and pulsed thermography in damaged CFRP and GFRP composite laminates. Preliminary raw thermographic images showed that the long pulse heating technique was more effective in retrieving flat bottomed hole defects with various diameters and in-depth location. Four post-processing techniques, including absolute thermal contrast, thermographic signal reconstruction, phase Fourier analysis and principal component analysis, were also applied to the three thermographic

techniques in order to enhance the quality of the defect image and reduce noise effects. Experimental results revealed that the highest damage detection performance was achieved by principal component analysis and long pulse thermography. In particular, only one defect with a depth/diameter ratio equal to 0.8 could not be detected on the GFRP test sample, whereas all material flaws at various in-depth location were identified on the CFRP specimen.

Acknowledgements

ZW would like to thank the financial support provided by the China Scholarship Council ref. "ZYGX2016J156". MM and FC acknowledge the Horizon 2020 "EXTREME" project and FC acknowledges the Royal Society-Newton Mobility Grant (IEC\NSFC\170387) to support this research work.

References

[1] Milne JM, Reynolds WN. The non-destructive evaluation of composites and other materials by pulsed video thermography. Pro Soc Photo- Opt Instrum Eng 1985:520:119-22.

[2] M. Omer, Q. Sultan. Post Processing of Thermographic NDT Data Using Dirac Comb. The Society for Experimental Mechanics. 2017; 41:179-190.

[3] Stephen D. Holland, Ricky S. Reusser. Material evaluation by infrared thermography. Annu.Rev.Mater.Res.2016;46:287-303.

[4] Markus Rahammer, Marc Kreutzbruck. Fourier-transform vibrothermography with frequency sweep excitation utilizing local defect resonances. NDT&E International.2017;88:83-88.

[5] Dionysopoulos, D., Fierro, G. P. M., Meo, M., Ciampa, F. Imaging of barely visible impact damage on a composite panel using nonlinear wave modulation thermography. NDT & E International 95, pp. 9-16, 2018.

[6] Fierro, G. P. M., Ginzburg, D., Ciampa, F., Meo, M. Imaging of barely visible impact damage on a complex composite stiffened panel using a nonlinear ultrasound stimulated thermography approach. Journal of Nondestructive Evaluation, 36(4), 69, 2017.

[7] Fierro, G. P. M., Ginzburg, D., Ciampa, F., Meo, M. Nonlinear ultrasonic stimulated thermography for damage assessment in isotropic fatigued structures. Journal of Sound and Vibration, 404, 102-115, 2017.

[8] He Y., Yang R., Zhang H., Zhou D., Wang G. Volume or inside heating thermography using

electromagnetic excitation for advanced composite materials. Int. J. Thermal Sci. 2017;111:41-49.

[9] Abidin, I. Z., Tian, G. Y., Wilson, J., Yang, S., & Almond, D. Quantitative evaluation of angular defects by pulsed eddy current thermography. Ndt & E International, 43(7), 537-546, 2010.

[10] Cheng, L., & Tian, G. Y. Transient thermal behavior of eddy-current pulsed thermography for nondestructive evaluation of composites. IEEE Transactions on Instrumentation and Measurement, 62(5), 1215-1222, 2013.

[11] Zhang H., Gao B., Tian G.Y, Woo W.L, Bai L. Metal defects sizing and detection under thick coating using microwave NDT. NDT&E International. 2013;60:52-61.

[12] Ciampa, F., Mahmoodi, P., Pinto, F. and Meo, M., Recent Advances in Active Infrared Thermography for Non-Destructive Testing of Aerospace Components. Sensors, 18(2), p.609, 2018.

[13] Pinto, F., Ciampa, F., Meo, M. and Polimeno, U. Multifunctional SMArt composite material for in situ NDT/SHM and de-icing. Smart Materials and Structures, 21(10), p.105010, 2012.

[14] Balageas DL. Defense and illustration of time-resolved pulsed thermography for NDE. Quantitative InfraRed Thermography Journal. 2012;9(1):3-32. Erratum: Quantitative InfraRed Thermography Journal. 2012;9(2):231.

[15] Balageas D, Chapuis B, Deban G, Passilly F. Improvement of the detection of defects by pulse thermography thanks to the TSR approach in the case of a smart composite repair patch. Quantitative InfraRed Thermography Journal. 2010;7(2):167-187.

[16] S. D. Holland, R. S. Reusser. Material evaluation by infrared thermography. Annual Review of Material Research, 2016;46(1): 287-303.

[17] Pickering, S. & Almond, D.: Matched excitation energy comparison of the pulse and lock-in thermography NDE techniques, NDT & E International 41, 501 – 509, 2008.

[18] Krankenhagen, R, Maierhofer Ch. Determination of the spatial energy distribution generated by means of a flash lamp. In: Proceedings of the 11th international conference on quantitative infrared thermography (QIRT 2012); p. 1–10, 2012.

[19] C. Meola, G. M. Carlomagno, A. Squillace et al., “Non-destructive evaluation of aerospace materials with lock-in thermography,” Engineering Failure Analysis, vol. 13, no. 3, pp. 380-388, 2006.

[20] Chatterjee, K., Tuli, S., Pickering, S. G., & Almond, D. P. (2011). A comparison of the pulsed,

lock-in and frequency modulated thermography nondestructive evaluation techniques. Ndt & E International, 44(7), 655-667, 2011.

[21] Badghaish AA, Fleming DC. Non-destructive inspection of composites using step heating thermography. J Compos Mater 2008;42:1337-57.

[22] Vavilov V P, Taylor R. Theoretical and practical aspects of the thermal nondestructive testing of bonded structures. Research Techniques in Nondestructive testing, 5. London: Academic Press; 1982; 239-79.

[23] Almond D P, Delpech P, Peng Wang, Behesty M. Quantitative determination of impact damage and other defects in carbon fiber composites by transient thermography. Proc SPIE. 1996;2944:256-64.

[24] Almond DP, Angioni SL, Pickering SG. Thermographic NDE advisory and guidance system. NDT&E International. 2016;83:134-42.

[25] Almond, D.P., Angioni, S.L. and Pickering, S.G. Long pulse excitation thermographic non-destructive evaluation. NDT & E International, 87, pp.7-14, 2017.

[26] Liang Cheng, Bin Gao, Gui Yun Tian, Wai Lok Woo, Gerard Berthiau. Imapact damage detection and identification using eddy current pulsed thermography through integration of PCA and ICA. IEEE Sensors journal.2014;14(5):1655-63.

[27] D.Griefahn, J. Wollnack, W. Hintze. Principal component analysis for fast and automated thermographic inspection of internal structures in sandwich parts. Journal of sensors and sensor systems. 2014;3;105-111.

[28] C. Ibarra-Castanedo, N. P. Avdelidia, M. Grenier, X. Maldague, A. Bendada. Active thermography signal processing techniques for defect detection and characterization on composite materials. Proc. of SPIE. 2010;7661:76610O.

[29] Bin Liu, Hai Zhang, Henrique Fernandes, Xavier Maldague. Quantitave evaluation of pulsed thermography, lock-in thermography and vibrothermography on Foreign Object Defect (FOD) in CFRP. Sensors, 2016;16(5):743.

[30] Vladimir P. Vavilov, Douglas D. Burleigh. Review of pulsed thermal NDT: Physical principles, theory and data processing. NDT&E International, 2015;73:28-52.

[31] Lopez, F., Maldague, X. and Ibarra-Castanedo, C., Enhanced image processing for infrared non-destructive testing. Opto-Electronics Review, 22(4), pp.245-251, 2014.

[32] M. Pilla, M. Klein, X. Maldague, A. Salerno. New absolute contrast for pulsed thermography.

QIRT 2002;53-58, 2002.

[33] Shepard, S.M.; Lhota, J.R.; Rubadeux, B.A.; Wang, D.; Ahmed, T. Reconstruction and enhancement of active thermographic image sequences. Opt. Eng. 42, 1337–1342, 2003.

[34] Roch J-M, Leroy F-H., Balageas DL. Image of TSR coefficients: a simple way for a rapid and efficient detection of defects. Materials Evaluation. 2013; 72(1):73-82.

[35] Daniel L. Balageas, Jean-Michel Roche. Common tools for quantitative time-resolved pulse and step-heating thermography-part I: theoretical basis. Quantitative Infrared Thermography. 2014; 11(1):43-56.

[36] J.-M. Roche, D. Balageas. Common tools for quantitative pulse and step-heating thermography -Part II: experimental validation[C], Quantitative Infrared Thermography Conference, 2014, 12(1): 1-23.

[37] Maldague, X.; Marinetti, S. Pulse phase infrared thermography. J. Appl. Phys. 79, 2694–2698, 1996.

[38] Marinetti, S., Grinzato, E., Bison, P. G., Bozzi, E., Chimenti, M., Pieri, G., & Salvetti, O. Statistical analysis of IR thermographic sequences by PCA. Infrared Physics & Technology, 46(1-2), 85-91, 2004.

[39] Rajic, N. Principal component thermography for flaw contrast enhancement and flaw depth characterisation in composite structures. Composite Structures, 58(4), pp.521-528, 2002.

[40] Winfree, W. P., Cramer, K. E., Zalameda, J. N., Howell, P. A., & Burke, E. R. Principal component analysis of thermographic data. In Thermosense: Thermal Infrared Applications XXXVII (Vol. 9485, p. 94850S). International Society for Optics and Photonics, 2015.

[41] Sakagami, T., & Kubo, S. Applications of pulse heating thermography and lock-in thermography to quantitative nondestructive evaluations. Infrared Physics & Technology, 43(3-5), 211-218, 2002.

[42] Vladimir P. Vavilov, Douglas D. Burleigh. Review of pulsed thermal NDT: Physical principles, theory and data processing. NDT&E International. 2015; 73:28-52.

[43] Miguel Lizaranzu, Alberto Lario, Agustin Chiminelli, Iban Amenabar. Non-destructive testing of composite materials by means of active thermography-based tools. Infrared physics & technology, 2015; 71:113-120.